Losartan-based nanocomposite hydrogel overcomes chemo-immunotherapy resistance by remodeling tumor mechanical microenvironment

Xiaodong Hou[1,2,3†], Yuting Shen[1,2,3†], Bin Huang[5†], Qiuyan Li[1,2,3], Shaoyue Li[1,2,3], Tingting Jiang[1,2,3], Xuexia Shan[1,2,3], Weichen Xu[1,2,3], Shuo Liu[1,2,3], Shengbo Wu[5], De Zhao[1], Anqi Zhu[1,2,3], Liping Sun[1,2,3*], Huixiong Xu[3,4*] and Wenwen Yue[1,2,3*]

Abstract

Preclinical studies demonstrating high cure rates with PD1/PD-L1 combinations have led to numerous clinical trials, but emerging results are disappointing. These combined immunotherapies are commonly employed for patients with refractory tumors following prior treatment with cytotoxic agents. Here, we uncovered that the post-chemotherapy tumor presents a unique mechanical microenvironment characterized by an altered extracellular matrix (ECM) elasticity and increased stiffness, which facilitate the development of aggressive tumor phenotypes and confer resistance to checkpoint blocking therapy. As thus, we rationally designed an in situ nanocomposite hydrogel system, LOS&FeOX@Gel, which enabled effective and specific delivery of the therapeutic payloads (losartan [LOS] and oxaliplatin [OX]) into tumor. We demonstrate that sustained release of LOS effectively remodels the tumor mechanical microenvironment (TMM) by reducing ECM deposition and its associated "solid stress", thereby augmenting the efficacy of OX and its immunological effects. Importantly, this hydrogel system greatly sensitized post-chemotherapy tumor to checkpoint blocking therapy, showing synergistic therapeutic effects against cancer metastasis. Our study provides mechanistic insights and preclinical rationale for modulating TMM as a potential neoadjuvant regimen for tumor to optimize the benefits of chemo-immunotherapy, which lays the groundwork for leveraging "mechanical-immunoengineering" strategies to combat refractory tumors. Graphical Abstract

†Xiaodong Hou, Yuting Shen and Bin Huang contributed equally to this work.

*Correspondence:
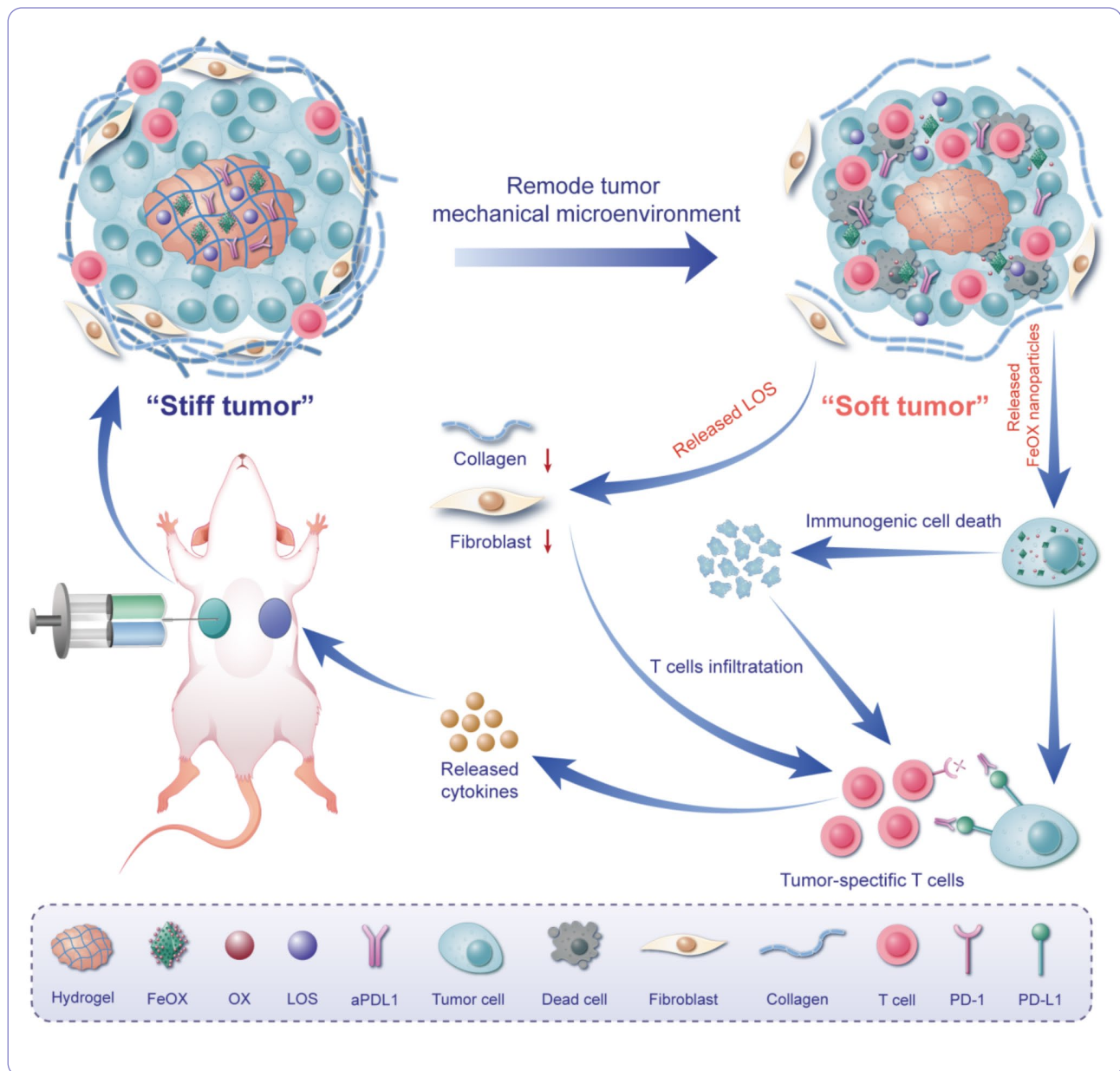Liping Sun
hxd984@163.com
Huixiong Xu
xuhuixiong@126.com
Wenwen Yue
yuewen0902@163.com

Full list of author information is available at the end of the article

Introduction

The development of immunotherapy, which targets immune checkpoint inhibitors (ICIs), has revolutionized the landscape of tumor treatment. Anti-PD1/PD-L1 agents serve as the backbone of the expanding approaches in the immuno-oncology field [1]. Monoclonal antibodies targeting the PD-1/PD-L1 pathway reactivate the functions of CD8+T cells, thus leading to tumor shrinkage. However, the overall response rate for anti-PD1/PD-L1 agents administered as monotherapy in cancer patients ranges merely from 20 to 30% [2–4]. The combination of anti-PD1/PD-L1 agents with some well-established therapeutic modalities (i.e., chemotherapy, radiotherapy, intervention and targeted therapy)

has been regarded as one of the most practical ways to improve immunotherapy response in cancer patients [5–7]. Unfortunately, despite promising preclinical evidence of the potential for combined immunotherapy to induce systemic antitumor immune responses, recent clinical trials have revealed that most patients do not experience durable benefits from these combinations [8, 9].

Cytotoxic chemotherapy continues to be a cornerstone of cancer treatment. More than 60% of cancer patients receive initial therapy with chemotherapeutics in addition to surgery, particularly among those with advanced-stage disease [10]. For most tumor types, such as breast cancer, ovarian cancer, and microsatellite-stable colon cancer, anti-PD1/PD-L1 agents are generally reserved

Hou *et al. Journal of Nanobiotechnology*   (2024) 22:667

Page 3 of 19

as a second- or third-line treatment option for patients who have not responded to prior treatments with cytotoxic agents, which exhibit significantly reduced efficacy in these cases [11, 12]. Emerging evidence indicates that patients who do not respond to standard chemotherapy often display a range of immunosuppressive characteristics within the tumor microenvironment (TME), including exhausted T cells, persistent regulatory T cells (Tregs), an increased B-cell population, and sustained populations of tumor-associated macrophages (TAMs) [13, 14]. In this context, the addition of ICIs is unlikely to yield significant clinical efficacy, highlighting the urgent need to identify the factors that contribute to the immunosuppressive microenvironment in tumors following long-term chemotherapy. And targeting these factors may facilitate remodeling of the TME and enhance sensitivity to anti-PD1/PD-L1 agents.

Previous studies underlined that the unique mechanical cues of the TME, such as altered extracellular matrix (ECM) elasticity or increased stiffness, not only affect the biological behavior of cancer cells but also interfere with the integrity of the cancer-immunity cycle [15–17]. Consequently, strategies targeting the tumor mechanical microenvironment (TMM) in order to improve the efficacy of immunotherapy are gaining momentum and represent an exciting direction for the field. Here in this study, based on the cases of triple-negative breast cancer (TNBC), our results showed that the high stiffness of tumor tissue was associated with several poor biological prognostic factors (i.e., a larger tumor size, more metastatic axillary nodes, high Ki67 expression and high a-SMA expression). Furthermore, based on a murine model of TNBC exposed to long-term chemotherapy, bioinformatics analyses revealed that ECM-associated genes *(i.e.*, Col26a1, Col8a2, Fgfrl, Fgf23, and Fcnb) were highly expressed in tumors following chemotherapy compared to treatment-naïve ones. Relatedly, the gene signature of the post-chemotherapy tumors, as revealed by transcriptome analysis, is strongly associated with resistance to PD-L1 checkpoint-blockade therapy in clinical settings. These findings underscore the profound alterations occurring within the TMM in response to aggressive chemotherapy, predominantly mediated by ECM remodeling and associated signaling pathways. These changes play a significant role in fostering aggressive tumor phenotypes and conferring resistance to diverse therapeutic interventions.

Losartan (LOS) is a US Food and Drug Administration (FDA)-approved antihypertensive drug with the primary structure of a low-molecular-weight (mw 461) non-peptide containing tetrazolium-substituted biphenyls and an imidazole ring structure [18]. In mouse models of breast cancer and pancreatic cancer, it has been demonstrated the ability to decrease the intratumoral expression of thrombospondin–1 (THBS–1), an activator of fibrogenic TGF-β, leading to a significant reduction in intratumoral collagen and hyaluronan content [19, 20]. The solid stress was consequently reduced, leading to alleviation of vessel compression and ultimately resulting in improved tumor mechanical forces [19, 20]. Also, tumor hypoxia was reduced and the delivery and efficacy of both low molecular-weight drugs and nanomedicine were enhanced [19–21]. These findings led to a successful phase II trial of LOS in combination with chemoradiation for the treatment of locally advanced pancreatic cancer [22]. Despite the potential of this therapy for cancer treatment, improving the effective utilization rate of drugs remains a primary focus.

Rapid expansion in the bioengineering and nanotechnology fields affords new approaches that could dramatically improve the safety as well as the therapeutic effectiveness of anti-cancer efficacy [6, 12, 23]. Notably, given that systemic administration of therapeutic agents would disrupt the homeostatic function of immune cells at the non-target tissues [24], the localized delivery vehicles can allow regulated and sustained release of payloads, thereby not only minimizing the off-target associated side effects but also enhancing efficient drug bioavailability [25–27]. Drawing on the aforementioned analysis, in this article we report an in situ injectable fibrin gel for locally synergistic delivery of LOS and Oxaliplatin (OX), a representative chemotherapeutic agent for tumor. The fibrin gel is a US FDA-approved material, and is formed by the interaction of fibrinogen and thrombin [28]. And biocompatible FeMOF nanoparticles grafted with RGD peptide were incorporated into the fibrin gel to function as a reservoir for controlled release of OX (FeOX), addressing various challenges such as short half-life, low bioavailability, and inadequate tumor targeting that limit its therapeutic efficacy. Based on a murine tumor model of post-chemotherapy treatment, we found that the fibrinogen solution containing LOS and FeOX nanoparticles and thrombin solution can be injected and mixed quickly within the tumor to form a hydrogel system (LOS&FeOX@Gel) in situ (Scheme 1). And the sustained release of LOS can effectively reshape TMM by reducing ECM deposition and its associated "solid stress". As thus, it further enhanced the anti-cancer efficacy and ICD effects of OX. With the synergism of the above two aspects, we verified that this injectable nanocomposite hydrogel system greatly enhances the sensitivity of post-chemotherapy tumors to ICIs treatment, and showed synergistic therapeutic effects against cancer recurrence and metastasis.

Hou *et al. Journal of Nanobiotechnology*   (2024) 22:667

Page 4 of 19
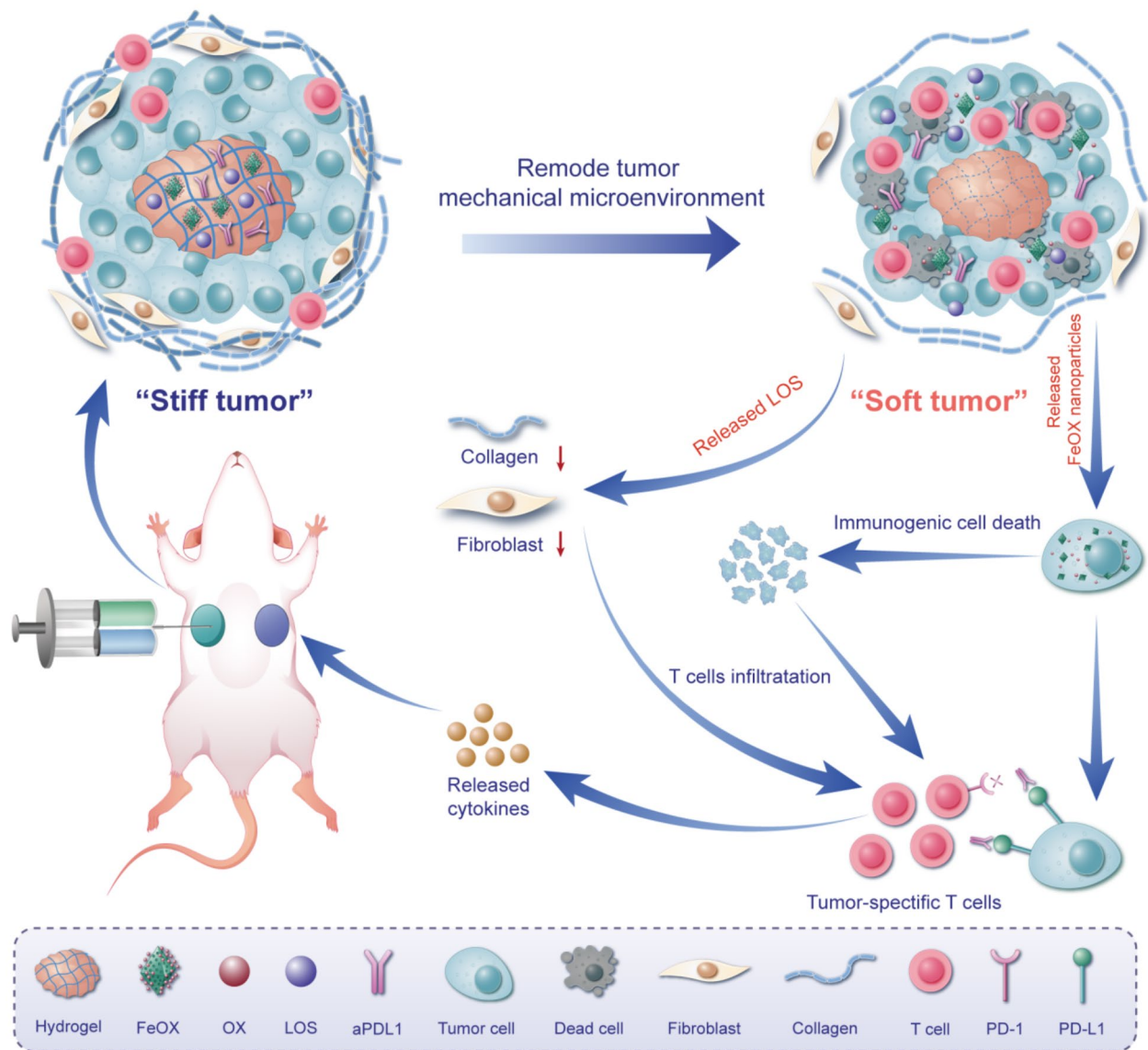
Scheme 1 Schematic of losartan-based nanocomposite hydrogel reshaping the tumor mechanical microenvironment to overcome chemo-immunotherapy resistance. The post-chemotherapy tumor presents a unique mechanical microenvironment characterized by an altered extracellular matrix (ECM) elasticity and increased stiffness. The injectable fibrin gel system in this strategy enables local retention and sustained release of therapeutic agents (Losartan [LOS] and FeOX), where LOS remodels the mechanical microenvironment by reducing the ECM and the associated "solid stress", further enhancing the anticancer efficacy of OX and its immunogenic cell death effect. With the synergism of the above two aspects, this injectable nanocomposite hydrogel system greatly sensitized post-chemotherapy tumor to checkpoint inhibitors therapy and shows synergistic therapeutic effects against recurrent and metastatic cancers. HMGB1, high mobility group box 1; CRT, calreticulin; aPDL1, anti-programmed death-ligand 1 blocking antibody; PD-L1, programmed death-ligand 1; PD-1, programmed death-1

Results and discussion

Altered mechanical microenvironment of the tumor after long-term chemotherapy plays a significant role in conferring resistance to checkpoint blocking therapy

Here, we firstly explored the association between tissue stiffness of tumors and biological prognostic factors in patients with TNBC. A total of 84 patients with TNBC confirmed by histopathologic examination from January 2018 to December.

2021 were analyzed retrospectively. Ultrasound shear wave elastography (SWE) examinations were performed for all patients (Fig. 1A). First, the assessment of the pathologic biomarker Ki67 by clinical pathologists was referenced in our study (Fig. S1), and the stiffness of the tumor in the region of interest (ROI) was assessed using SWE imaging. The comparison of tissue stiffness across different biological prognostic factors was conducted (Fig. 1B). And our results showed that the high tissue stiffness was associated with several poor biological
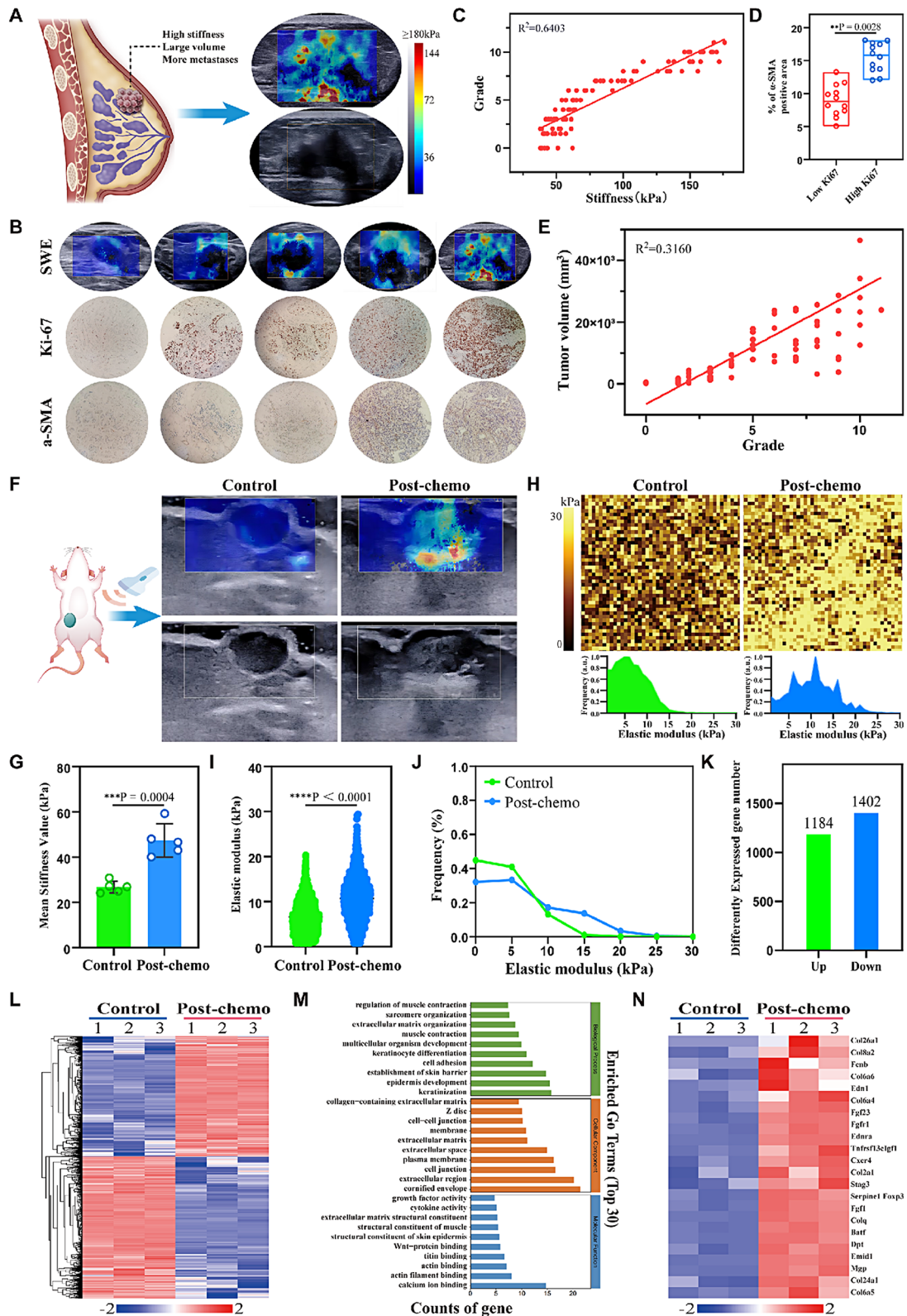
Fig. 1 (See legend on next page.)

Hou *et al. Journal of Nanobiotechnology*   (2024) 22:667

Page 6 of 19

(See figure on previous page.)

Fig. 1 The chemotherapy-induced alterations in the tumor mechanical microenvironment facilitate the development of aggressive tumor phenotypes and confer resistance to diverse therapeutic interventions. (**A**) Representative elastic modulus diagram of triple-negative breast cancer (TNBC) patients. (**B**) Representative elastic modulus diagram of TNBC patients and pathograms corresponding to Ki67, a-SMA of immuno-histochemical (IHC) (Scale bar: 500 µm). (**C**) Linear fit analysis of stiffness of the tumor tissues to pathology scores in scatter plots ($n = 84$). (**D**) Quantification of a-SMA biomarker in IHC sections in low and high Ki67-expressing TNBC patients. Quantification of a-SMA by Image J software. (**E**) Linear fit analysis of patient pathology scores to tumor volumes in scatter plots. The data distribution was shown as a histogram ($n = 84$). (**F**) Elastic modulus of post-chemotherapy tumors and control group by SWE in the corresponding mouse models. (**G**) Quantitative results of ROI in SWE images of tumors in different groups ($n = 5$ mice). (**H**) Typical force maps of atomic force microscopy (AFM) measurements of extracted tumors from post-chemotherapy and control group ($n = 3$; 250 measurements for each condition, 10 conditions for each sample). (**I**) Elastic modulus of post-chemotherapy and control group tumors measured by AFM. (**J**) The corresponding histograms for AFM measurements of post-chemotherapy and control group tumors. (**K** and **L**) Column plot and Venn diagram of differentially expressed genes in RNA-sequencing between post-chemotherapy and control group ($n = 3$ mice). (**M**) Significant enrichment in Gene Ontology (GO) terms (top 30, $n = 3$ mice). (**N**) Heat map of differentially expressed genes correlated with tumor proliferation and immunosuppression ($n = 3$ mice). G, I Data were presented as the mean $\pm$ SD ($n = 5$ biologically independent samples). Statistical significance was calculated by the two-tailed unpaired Student's t-test. **$P < 0.01$, ***$P < 0.001$,****$P < 0.0001$

prognostic factors (i.e., a larger tumor size, more metastatic axillary nodes, higher Ki67 and a-SMA expression) for patients with TNBC (Fig. 1C-E and S2). These findings highlight the significant role of mechanical properties in affecting the biological behavior of cancer cells, and provide insights into the accquired resistance to various therapeutic interventions following long-term chemotherapy.

To investigate the mechanical alterations in tumors exposed to long-term chemotherapy, a preclinical post-chemotherapy TNBC mouse model was introduced in this study. Firstly, the TNBC mouse was constructed using a low-dose DOX (5 mg/kg) induction method to mimic clinically acquired resistance, and the residual tumors were then inoculated into the breast fat pads of 6–8 week old female mice [29]. Ten days after inoculation of the tumors, SWE was performed every 2 days and tumor burden was monitored. As indicated in Fig. 1F, g, the tissue stiffness of post-chemotherapy tumor was significantly higher than that of control group. A comprehensive dissection of mechano-surveillance mechanisms inevitably relies on precise methods for measuring forces. A large number of in vitro techniques, such as atomic force microscopy (AFM)) and biomembrane force probe, have become available to measure the mechanical properties of single cells, tissues, and cell-cell interaction forces [5, 30]. AFM enables the evaluation of quantitative stiffness measurements through higher spatial resolution imaging and cell mechanics, and the tissue stiffness of the tumor at the subcellular level was also evaluated by AFM. Correspondingly, the high-resolution AFM maps showed that the post-chemotherapy tumor exhibited greater elastic modulus and stiffness heterogeneity compared to control group (Fig. 1H, I,J). The data revealed the development of a highly stiff phenotypic state in tumors upon exposure to aggressive chemotherapy.

To further explore the underlying mechanism of the promoted tumor progression effects of the unique mechanical cues of the TME, we conducted RNA-seq analysis for tumors 20 days after inoculation. As expected, the results presented that the gene expression profiles of post-chemotherapy tumors were significantly different from that of control group, with a total of 2586 differentially expressed gene profiles between two groups (Fig. 1K, L and S3A). Furthermore, gene ontology (GO) analysis was performed, including biological processes, cellular components, and molecular functional immunity (Fig. 1M). Among them, the top enriched terms included extracellular matrix organization, keratinization, cell adhesion in the mechanical process, collagen-containing extracellular matrix, extracellular matrix, extracellular space and cornified envelope in the cellular component. Notably, the genes (i.e., Col26a1, Col8a2, Fgfrl, Stag3) encoding collagen, fibroblasts, and stromal antigen were found to be significantly overexpressed in post-chemotherapy tumors (Fig. 1N). The genes which are highly correlated with PD-L1 resistance in clinic (i.e., Cd3e [31], Batf [32, 33], ALK [34, 35]) were significantly overexpressed in the post-chemotherapy tumors (Fig. S3B). Based on the multiple immuno-histochemical (IHC) assay, we also found higher levels of expression of α-SMA-positive stromal cells and collagen-I in the post-chemotherapy group compared with the control group, which corresponded to the results of transcriptomics analysis (Fig. S4A-D). Taken together, the above findings suggest the establishment of a distinct TMM characterized by modified ECM elasticity and heightened stiffness in tumors subjected to long-term chemotherapy, which contributes to tumor immunosuppression and confers resistance to ICIs treatment. Thus, it suggested that targeting TMM should likely play a vital role in enhancing the treatment efficacy of existing ICIs therapies.

Construction of LOS@Gel system to reshape TMM of the post-chemotherapy tumors

As previously mentioned, several studies have reported that LOS has the ability to effectively reduce collagen and hyaluronic acid content within tumors, alleviate solid stress, and mitigate vascular compression in mouse models of breast and pancreatic cancer [12, 22]. And the natural biomaterial fibrin gel, which has already been used clinically for hemostatic therapy, is employed in

this work to encapsulate LOS (LOS@Gel) that enables sustained drug release to achieve optimal therapeutic outcomes (Fig. 2A). The hydrogel system was prepared through admixing fibrinogen and thrombin solutions in a 2:1 volume ratio with a double tube syringe (Fig. 2B). The porous network microstructure of this hydrogel system was obtained by cryo−scanning electron microscopy (Cryo-SEM) analysis (Fig. 3C). The character of hydrogel was evaluated by using a rheology analysis including elastic (G′) and viscous (G″) moduli. As expected, G′ was rapidly increased with thrombin addition to fibrinogen solution, proving that the strength of hydrogel was well-improved (Fig. 2D and E), and the addition of LOS did not alter the properties of the hydrogel system(Fig. S5A-C). The integrity of the fibrin gel could be maintained for at least 1 week, and gradually degraded until the 3th week (Fig. S6). In addition, the hydrogel system in vivo also could be maintained for almost 7 days, and its size gradually diminished over time (Fig. 2F). On day 28 after injection, the gel completely disappeared without any obvious inflammatory effect as shown in hematoxylin and eosin (H&E) staining test, indicating the optimal biocompatibility and biodegradability of this hydrogel system (Fig. 2F). Also, as shown in Fig. 2G-I, the fibrin gel enabled sustained slow release of the loaded therapeutics both in vitro and in vivo. Collectively, benefiting from the high biosafety and the well drug release properties, hydrogels utilized in this study should maximize LOS utilization and improve its therapeutic effects.

According to Hu's report, the utilization of LOS-loaded hydrogel in the 4T1 mouse model effectively modulates cancer-related fibroblasts through sustained release of LOS, thereby enhancing chemotherapy efficacy and suppressing tumor growth [31]. To determine whether in situ formation of LOS-loading fibrin gel could reshape the mechanical microenvironment of the post-chemotherapy tumor. PBS, blank gel, single free LOS, sequential free LOS or LOS@Gel were injected at the peritumoral sites, respectively. Fourteen days after the treatment, SWE imaging was performed (Fig. 2J). Our results revealed that LOS@Gel and sequential free LOS significantly reduced the stiffness of tumors, while blank gel, single free LOS did not effect the stiffness of tumors compared to PBS-treated group (Fig. 2J, Fig. S7A and Fig. S8A, B). To compare the microscopic stiffness, AFM tests were performed on the corresponding tumor specimens. Blank gel, single free LOS failed to reduce the mean elastic modulus of tumors compared to control group, while the mean elastic modulus of tumors in mice was significantly decreased due to the sustained release of LOS from LOS@Gel (Fig. 2K and S7B). The elastic modulus distribution of LOS@Gel-treated tumors exhibited a general shift towards lower values compared to the control

group, while higher range values were not observed (Fig. S7C, Fig. S8C).

To further investigate the potential mechanism by which LOS@Gel reshaped TMM of the post-chemotherapy tumors, tumor tissues were collected and subjected to multiplex immunohistochemical (mIHC) analysis on the 14th day following various treatments. We found that application of LOS@Gel significantly reduced the number of a-SMA-positive stromal cells, accompanied by a notable decrease in the levels of collagen-I, while blank gel, single free LOS did not effect the content of a-SMA-positive stromal cells and collagen-I in post-chemotherapy tumors (Fig. 2L, S8C, D and Fig. S9A, B). Furthermore, our findings indicate that LOS@Gel administration significantly enhances the proportion of perfused vessel area (Fig. 2L and S9C). This can be attributed to the sustained release of LOS, which effectively mitigates tumor solid stress and subsequently reduces vascular pressure while improving vascular perfusion. Taken together, LOS@Gel system reshaped a unique TMM characterized with an altered ECM elasticity and increased stiffness.

LOS@Gel enhancing the anticancer efficacy of OX and its immunogenic cell death

Considering the superior performance exhibited by the LOS@Gel, we conducted further investigations to determine its potential as an effective chemosensitization agent for tumor. To enhance the utilization rate of chemotherapeutic agent, FeMOF that has the advantages of large specific surface area, easy modification, high loading efficiency and excellent biocompatibility, was introduced in this study [36]. And we developed OX-encapsulated FeMOF-based nanocarriers. Self-assembled synthesized FeMOF nanoparticles were clearly shown as octahedral structure with uniform size and excellent dispersion under transmission electron microscope (TEM) (Fig. 3A, and B). Elemental mapping was conducted to analyze the presence and uniform distribution of Fe, O, N and C elements (Fig. 3C and D).The characteristic graphs of the synthesized FeMOF crystals were identical to the simulated graphs of the Cr-doped MIL-101 (Cr) structure (Fig. 3E), indicating that the preparation of FeMOF nanoparticles was successful. X-ray photoelectron spectroscopy (XPS) was further carried out for surface structural characterization, indicating successful assembly of FeMOF (Fig. 3F and S10A-C). To enhance in vivo targeting and intracellularization, RGD peptide was grafted to FeMOF. And an additional peak at 2081 cm^{-1} was observed in fourier transform infrared (FTIR) spectroscopy due to the presence of the tyrosine of the RGD polypeptide, which indicated the successful grafting of the RGD peptide (Fig. S10D). While FeMOF grafted with RGD exhibited a slight increase in hydrodynamic
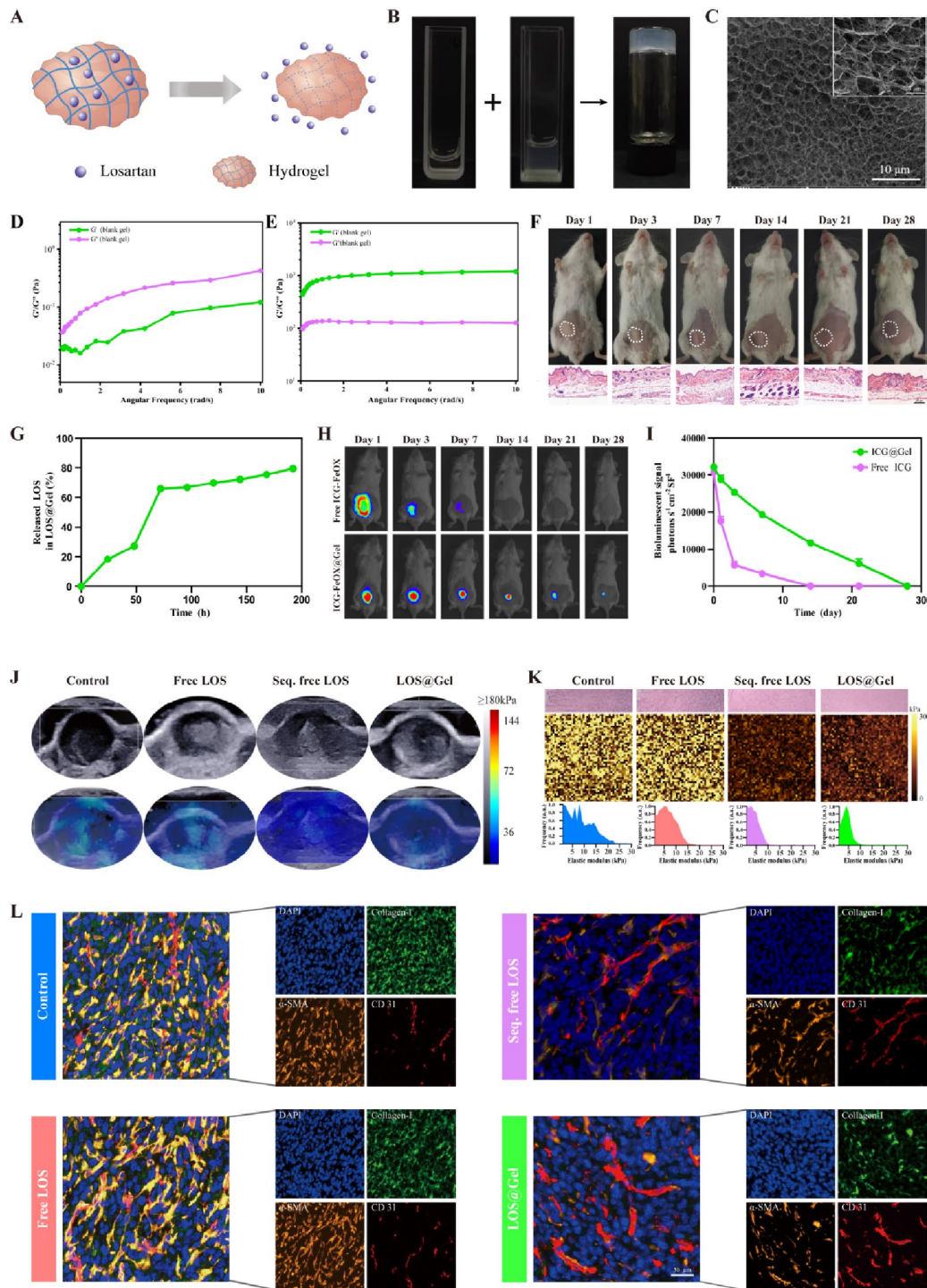
Fig. 2 Sustained release of LOS in hydrogel system reshapes the mechanical microenvironment of the post-chemotherapy tumor. (**A**) Schematic representation of the release of LOS encapsulated in fibrin gel formed in situ. (**B**) Photograph of the fibrin gel formation. (**C**) Representative cryo-scanning electron microscopy (Cryo-SEM) of blank fibrin gel. (**D**, **E**) Frequency rheological behavior of blank fibrin gel. (**F**) The photographs of the degradation process of fibrin gel in vivo by H&E staining. (**G**) Cumulative release curves of LOS from fibrin gel incubated with 1×PBS solution. data are mean±SD (*n*=3). (**H**) Fluorescence imaging monitored the residence of free ICG and ICG@Gel at the indicated time points in vivo. (**I**) The retention and accumulation curves of free ICG and ICG@Gel measured by fluorescence intensity at different time points after in situ injection in vivo. (**J**) Representative SWE images of the tumors from control, single free LOS, sequential free LOS and LOS@Gel treatment groups. (**K**) Typical force maps of AFM measurements of extracted tumors from different treated tumor bearing mice (*n*=3; 250 measurements for each condition). (**L**) Representative mIHC stained images showing a-SMA, collagen-I and CD31 of tumors extracted from different treatment
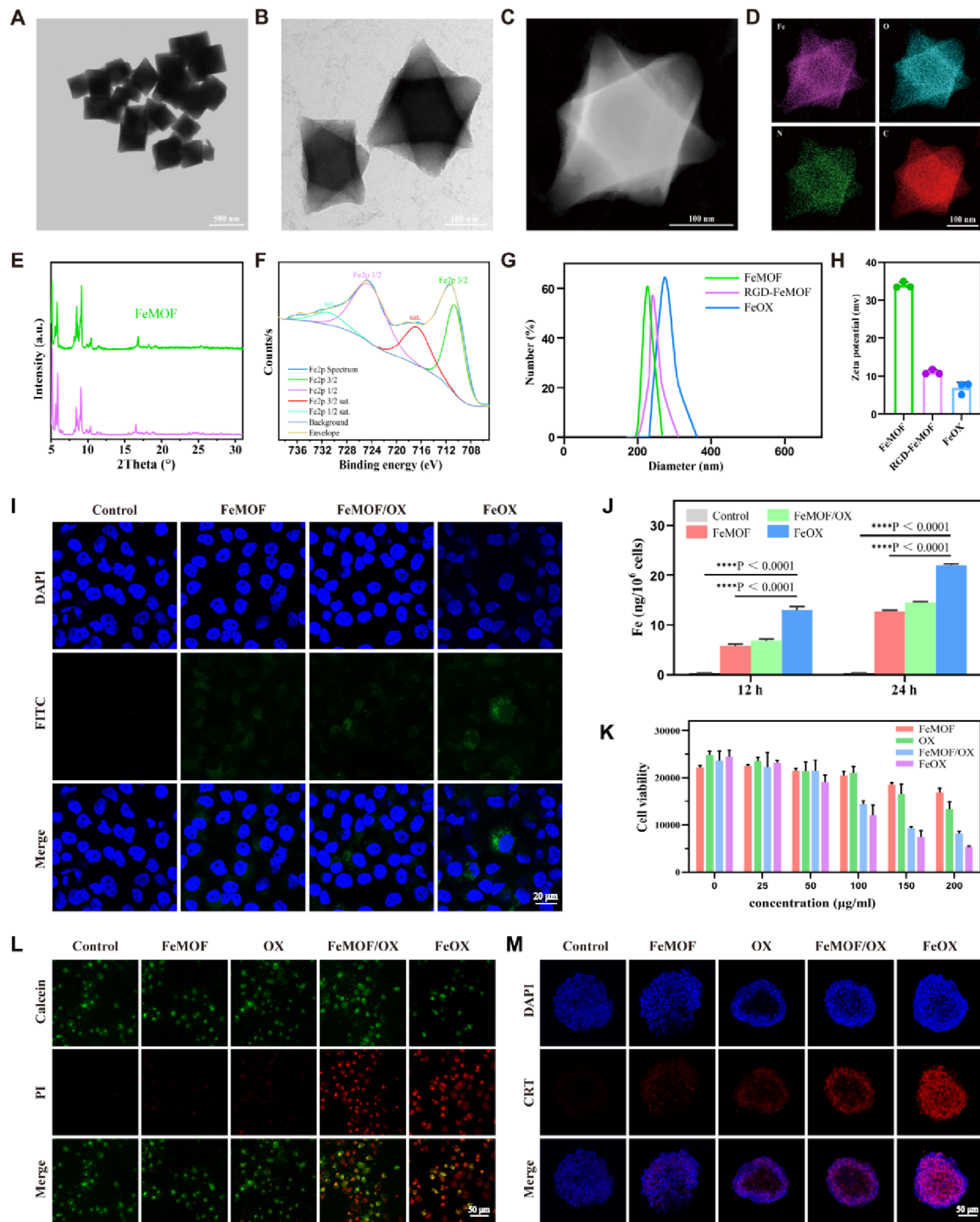
Fig. 3 Characterization of FeMOF-based nanoplatform and cytobiological functions of FeOX nanoagents in vitro. (**A**, **B**) Transmission electron microscopy (TEM) images of FeMOF. (**C**) Secondary electronic image of a single FeMOF. (**D**) The representative EDS elemental mappings of FeMOF nanoparticles. (**E**) XRD spectrum of FeMOF powder with MIL-101(Cr) as a modelled reference. (**F**) High-resolution X-ray photoelectron spectroscopy (XPS) spectra of Fe2p for FeMOF. (**G**,**H**) Hydrodynamic size (**G**) and zeta potential (**H**) of FeMOF before and after RGD modification. (**I**) Representative CLSM images of MCF-7/ADR cellular uptake after incubation with various samples for 24 h. (**J**) ICP assay for intracellular iron levels after MCF-7/ADR cells co-culture treatment with various samples for 12–24 h. (**K**) CCK-8 Kits to assess the viability of MCF-7/ADR cells cocultured with specific concentrations of various samples for 24 h. (**L**) Representative CLSM observation apoptosis levels of MCF-7/ADR cells incubated with various samples for 24 h. (**M**) Representative CLSM images of MCF-7/ADR multicellular spheroid cells incubated with various samples and stained with CRT antibodies. J, Data were presented as the mean ± SD ($n = 3$ biologically independent samples). Statistical significance was calculated by the two-tailed unpaired Student's t-test. ***$P < 0.001$, ****$P < 0.0001$

diameter and a decrease in surface charge (Fig. 3G and H). After the drug OX loading, FeOX still remains an octahedral structure consistent with FeMOF, exhibiting uniform size and excellent dispersion under TEM (Fig. S11A, B). The hydrodynamic diameter increased to 267.2 nm and the surface charge decreased to 8.6 mV after the drug OX loading (Fig. 3G and H). The encapsulation efficiency was calculated to be 43.07% according to the high performance liquid chromatography (HPLC) determination (Fig. S12).

The inherent particle size structure of FeMOF could easily disintegrated when exposed to reducing molecules like glutathione [37, 38]. To validate the degradastion of FeMOF in a simulated tumor environment in vitro, we systematically monitored the time-course concentration of the released iron species (Fig. S13A) and measured the release of iron at different time points using inductively coupled plasma mass spectrometry (ICP-MS) (Fig. S13B). Our findings indicate that under weakly acidic conditions, there is a slight degradation of the samples, accompanied by a minimal release of iron. In contrast, the presence of GSH significantly accelerates the degradation process and enhances the release of iron. To evaluate the efficiency of FeOX nanoagents uptake by tumor cells, a series of samples were labeled with fluorescein isothiocyanate (FITC), incubated with MCF-7/ADR cells for 24 h, and analyzed by confocal laser scanning microscopy (CLSM). Due to the RGD modification, MCF-7/ADR cells incubated with FeOX exhibited significantly stronger FITC fluorescence compared to the original FeMOF and FeMOF/OX (Fig. 3I). In addition, the intracellular iron accumulation induced by the nanoagents was highly consistent with FITC fluorescence, where the iron concentration in FeOX group increased by 52% compared to FeMOF/OX and 74% to FeMOF, detected by inductively coupled plasma masss spectrometry (ICP-MS) (Fig. 3J). The results suggest that FeOX exhibits a high affinity for tumor cells, providing the integrated benefits of improved circulatory stability and enhanced tumor targeting.

OX has been extensively utilized in the treatment of TNBC and has been demonstrated to induce ICD by exposing cell-surface CRT and releasing HMGB1 into the extracellular medium [39–41]. As shown in Fig. 3K and L, after treating the MCF-7/ADR cells with FeOX for 24 h, FeOX significantly inhibited MCF-7/ADR cell viability in a concentration-dependent manner. Moreover, we observed a significant increase in HMGB1 release from the nucleus, and the expression of cell surface CRT was significantly upregulated, in sharp contrast to control groups (Fig. 3M and S14). Taken together, these findings suggested that FeOX nanotherapeutic agent exhibit superior efficacy compared to free chemotherapy strategy and significantly augmenting immunogenicity of the OX.

Encouraged by the superior capability of FeOX nano-chemotherapy in vitro, we wondered whether LOS@Gel-augmented chemotherapy would have certain effect on the tumor in vivo. Tumor-bearing mice were implanted peritumorally with PBS, FeMOF@Gel, LOS@Gel, FeOX@Gel, LOS&FeOX@Gel (dose of FeMOF = 10 mg kg^{-1}, LOS = 60 mg kg^{-1} and OX = 10 mg kg^{-1}). Tumor growth was monitored every two days. We observed that FeMOF@Gel and LOS@Gel showed similar effects, but not showed a partial delay in tumor growth, all of them died within 40 days. Of note, mice treated with LOS&FeOX@Gel exhibited significant tumor suppression, with 100% of them survived for at least 40 days (Fig. 4F). When investigating a particular combination therapy, it is always worth considering the possible side effects. In this study, LOS&FeOX@Gel had no significant effect on the average body weight of mice (Fig. 4G). After 10 and 20 days treatment, histological analysis of the major better than the untreated controls (Fig. 4A-E). Although mice treated with FeOX@Gel organs of the mice showed no obvious pathological abnormalities compared with that of the untreated healthy mice (Fig. S15A). Furthermore, all serum biochemical parameters measured at different time points were normal in mice treated with LOS&FeOX@Gel, indicating that this topical combination therapy strategy did not cause significant toxic effects (Fig. S15B).

Mechanism of the synergistic antitumor responses

To further elucidate the potential mechanism of antitumor responses induced by LOS&FeOX@Gel system, all tumor tissues were harvested after two weeks treatment, and mIHC staining and flow cytometry ananlysis were performed on the tumor tissues. Considering the immunological effects induced by FeOX in vitro, it was further employed for in vivo evaluation. We also investigated the role of intratumoral immune cells in mediating the therapeutic effects of LOS&FeOX@Gel when the mechanical microenvironment of tumor was reshaped. Similar to the in vitro results, abundant HMGB1 and CRT expressions were detected on tumors after FeOX@Gel treatment (Fig. 5A). And the administration of LOS@Gel-augmented chemotherapy resulted in a significant increase in the levels of HMGB1 and CRT, which were favorable for eliciting antitumor immune responses. Accordingly, we evaluated changes in the intratumoral leukocyte phenotypes by flow cytometry. We found that LOS&FeOX@Gel treatment significantly increased the frequency of tumor-infiltrating CD8$^+$T cells (CD45$^+$CD3$^+$CD4$^-$CD8$^+$) but not CD4$^+$T cells (CD45$^+$CD3$^+$CD4$^+$ CD8$^-$) (Fig. 5B, D). In addition, Tregs were significantly reduced in tumors (Fig. 5C, E). Correspondingly, CD8/Treg, an indicator of antitumor immune homeostasis, was remarkably
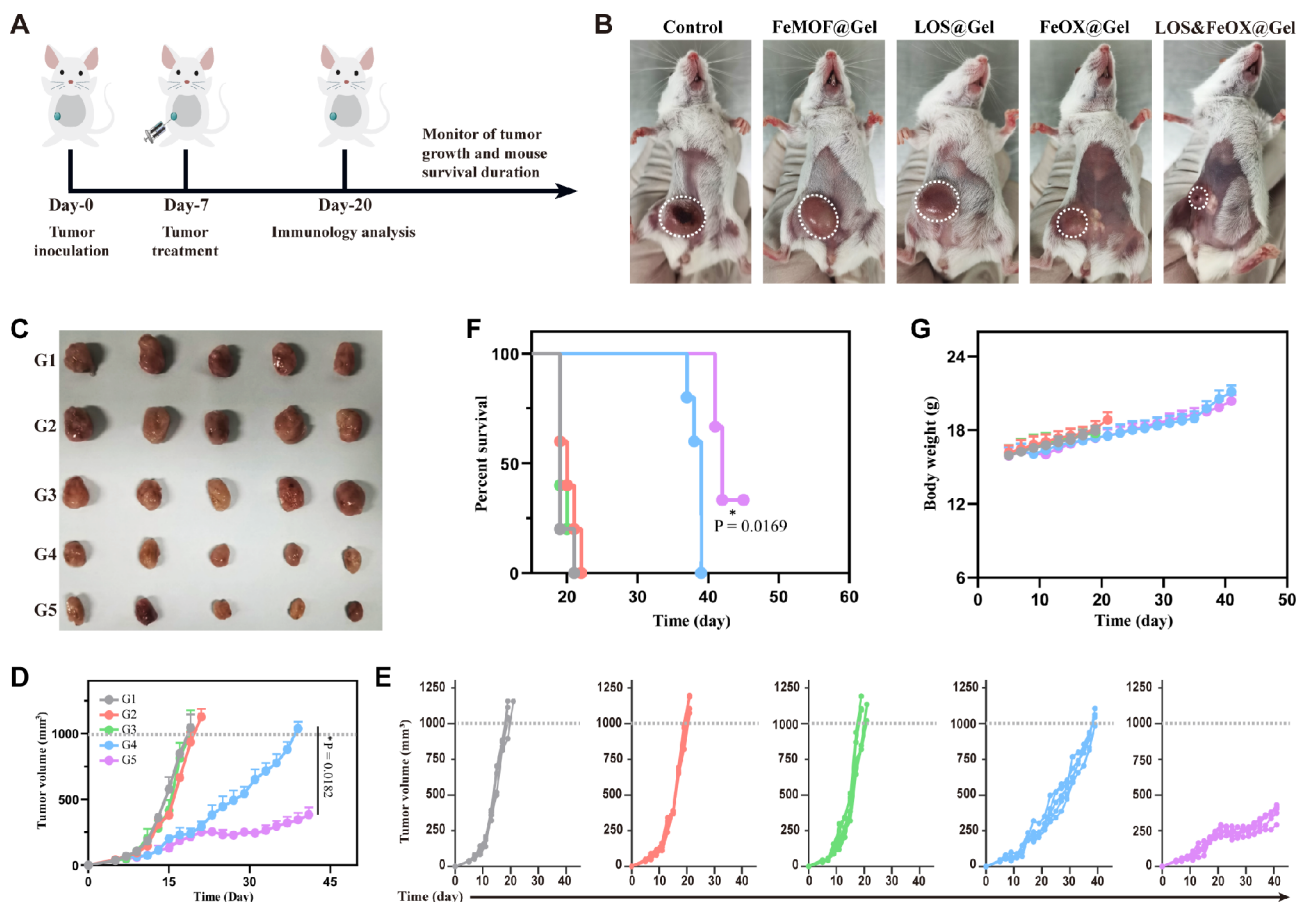
Fig. 4 Effects of LOS@gel-enhanced chemotherapy against tumor in vivo. (**A**) Schematic diagram of the treatment schedule in tumor bearing model with unilateral tumor. (**B**) Representative photographic imaging of different groups of mice after 14 days of varied treatments. (**C**) In vivo representative photographic imaging of different groups of mice after varied treatments as indicated. (**D**-**F**) Mean tumor growth curves (**D**), individual tumor growth kinetics (**E**), Kaplan-Meier survival curves (**F**), body weight fluctuation curves (**G**) in tumor-bearing mice after varied treatments (*n* = 5 mice in D-F). G1, Control; G2, FeMOF@Gel; G3, LOS@Gel; G4, FeOX@Gel; G5, LOS&FeOX@Gel. D, Data are presented as the mean ± SD (*n* = 5). Statistical significance was calculated by the two-tailed unpaired Student's t-test. F, Survival analysis determined by the log-rank (Mantel-Cox) test. *$P < 0.05$

ameliorated in the LOS&FeOX@Gel treatment group (Fig. S17).

The antitumor immunity was further verified by the mIHC analysis. It has been found that LOS&FeOX@Gel instigated CD8$^+$T cells infiltration into the tumors. Also, the Ki67 expression was significantly reduced in the treated group, demonstrating that the combination therapy effectively impeded tumor proliferation (Fig. 5F), the levels of tumor necrosis factor-α (TNF-α) and interferon-γ (IFN-γ) were highest in serum of mice treated with LOS&FeOX@Gel (Fig. 5G, H), which again indicated LOS&FeOX@Gel could trigger a strong immune response. The data presented here suggest that LOS&FeOX@Gel exploits mechanical microenvironment remodeling to enhance the effectiveness of OX-induced ICD and facilitate augmented infiltration of CD8$^+$ T cells into the tumor. Consequently, it effectively elicits antitumor immune responses and suppresses the growth of the tumors.

LOS&FeOX@Gel renders the post-chemotherapy tumor responsive to checkpoint immunotherapy

Given that tumor metastasis is the primary cause of cancer-related mortality, and chemoresistant tumor represents an exceptionally aggressive form of metastatic disease, an optimal therapeutic approach should not only target the primary lesion but also effectively inhibit metastasis [42, 43]. The field of ICIs-based immunotherapies has experienced significant advancements in recent years, yielding promising clinical outcomes. The integration of PD-1/PD-L1 checkpoint blockade therapies with other therapeutic modalities has garnered substantial interest across diverse research domains [23]. The expression of PD-L1 in tumors was assessed both before and five days after treatment with LOS&FeOX@Gel. The expression of PD-L1 in tumors was assessed both before and five days after treatment with LOS&FeOX@Gel. Our findings demonstrate that the administration of LOS&FeOX@Gel effectively enhances PD-L1
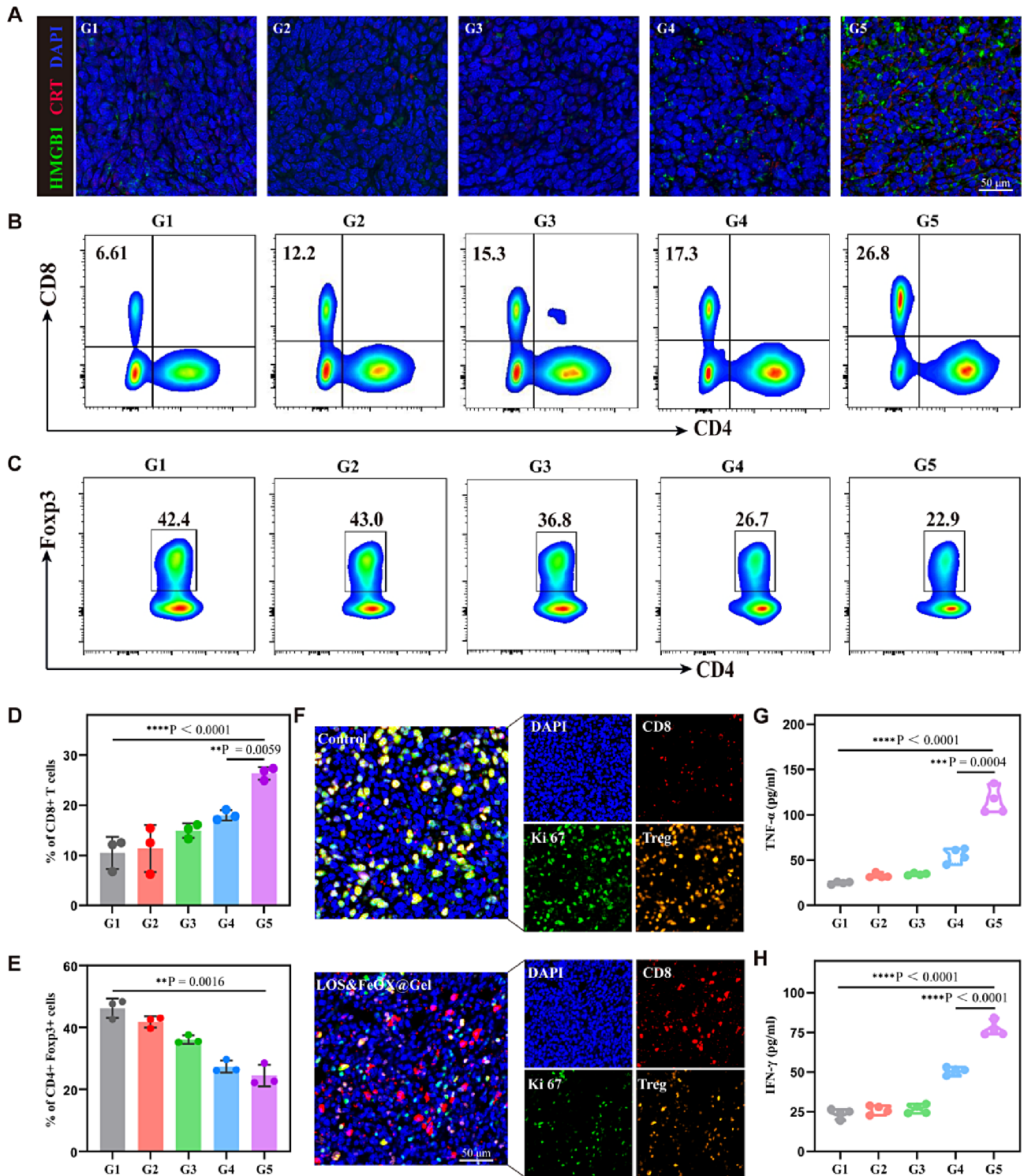
Fig. 5 Mechanism of the synergistic antitumor responses. (**A**) Representative mIHC staining images of tumor tissue sections with DAPI (blue), CRT (red), HMGB1 (green) cell infiltration in tumors after varied treatments. (**B**, **C**) FCM analysis of the frequency of CD8$^+$ T cells in CD45$^+$CD3$^+$ cells (**B**) and CD4$^+$Foxp3$^+$ Treg cells in CD3$^+$ cells (**C**) in tumors after varied treatments. (**D**, **E**) Quantification by FCM of CD8$^+$ T cells (**D**), CD4$^+$Foxp3$^+$ Treg cells (E). (**F**) Representative mIHC staining images of tumor tissue sections with DAPI (blue), CD8$^+$ T (red), Treg(yellow) and Ki67(green) cell infiltration in tumors after varied treatments. (**G**, **H**) Cytokine levels of TNF-α (g) and IFN-γ (h) in the serum after varied treatments. G1, Control; G2, RGD-FeMOF@Gel; G3, LOS@Gel; G4, FeOX@Ge; G5, LOS&FeOX@Gel. **D,E** Data are presented as the mean ± SD (*n* = 3). G, H Data are presented as the mean ± SD (*n* = 4). Statistical significance was calculated by the two-tailed unpaired Student's t-test. **$*P$ < 0.01, $***P$ < 0.001, $****P$ < 0.0001

expression in tumor xenografts in vivo, as confirmed by immunofluorescence analysis (Fig. S19A, B). These results provide direct evidence supporting the selection of aPD-L1 for combination therapy. To investigate the synergistic tumor suppression efficiency of the integrated PD-L1 blocked therapy with LOS&FeOX@Gel, a mouse model of bilateral tumor-bearing was employed. Five days after inoculation of the primary tumor (right), a second tumor was implanted on the left to simulate a distant tumor (Fig. 6A). On day 7, the right primary tumors were implanted peritumorally with αPDL1@Gel, LOS&FeOX@Gel, αPDL1&LOS &FeOX@Gel (dose of αPDL1=3.75 mg kg^{-1}, LOS=60 mg kg^{-1} and OX=10 mg kg^{-1}). Therapeutic results indicated that αPDL1 alone indeed had no significant inhibitory effect on either primary or distant tumors Fig. 6B-E and S19A, B), demonstrating that the tumor was resistant to ICIs therapy. Although LOS&FeOX@Gel could inhibit the growth of primary tumors to some extent, the ability to inhibit distant tumors was relatively tenuous. Remarkably, LOS&FeOX@Gel combined PD-L1 blockade not only inhibited the growth of in situ tumors, but also significantly suppressed the growth of distant tumors. In addition, no abnormal weight loss was observed in mice of the αPDL1&LOS &FeOX@Gel group (Fig. 6F).

In order to illuminate the immunotherapeutic mechanism of LOS&FeOX@Gel combined with αPDL1, immune cells in the distant tumors were evaluated on day 20. The results of the FCM analysis showed that the proportion of CD8$^+$ T (CD45$^+$CD3$^+$ CD4$^-$CD8$^+$) cells in the tumors of the αPDL1&LOS&FeOX@Gel group was significantly increased (Fig. 6G, I). Meanwhile, the frequency of Treg cells was significantly decreased in distal tumors in the combination treatment group (Fig. 6H, J). As a result, the CD8/Treg ratio was significantly improved in LOS&FeOX@Gel plus αPDL1 group (Fig. 6K). In support, the above results were also endorsed by mIHC (Fig. 6L). Furthermore, the proliferation index (displayed by Ki67 staining) of tumor in the combined treatment group was much higher than that of non-treated tissue. Moreover, LOS&FeOX@Gel plus αPDL1 elicited the highest levels of serum cytokine (i.e., TNF-α and IFN-γ) secretion compared to all other controls (Fig. 6M, N).These results demonstrated that LOS&FeOX@Gel renders post-chemotherapy tumor responsive to checkpoint immunotherapy, and the combination of LOS&FeOX@Gel with αPDL1 treatment can be further enhanced to induce a potent synergistic antitumor immune response, which is essential for eliciting the abscopal effect.

Conclusion

In summary, our findings reveal that chemotherapy-induced alterations in the mechanical characteristics of the TME facilitate the development of aggressive tumor phenotypes and confer resistance to diverse therapeutic interventions. Accordingly, we designed an in situ nanocomposite hydrogel system, LOS&FeOX@Gel, that enables the steady release of LOS and targets OX delivery into the tumor. Sustained release of low-dose LOS treatment mitigates tumor solid stresss and improves vascular perfusion, which facilitates the remodeling of the tumor TMM. This process ultimately enhances the anti-cancer efficacy of OX/αPDL1-based chemo- immunotherapy. Also, our study provided mechanistic insights and preclinical rationale for modulating the TMM as a neoadjuvant regimen for tumor to achieve the maximum clinical benefit of chemo-immunotherapy, which lays the groundwork for leveraging "mechanical immunoengineering" strategies to combat refractory tumors.

Materials and methods
Materials
All the chemicals used in our studies were sourced from Sigma-Aldrich unless otherwise stated. NHS-PEG-MAL was purchased from JenKem Technology CO., Ltd. c(RGDyC) peptide was obtained from Chinese peptide company. Losartan was obtained from APExBIO (Catalog No.B1072/114798-26-4). Oxaliplatin was obtained from Aladdin (Catalog No.61825-94-3). Fibrinogen and thrombin were abtained from Solarbio (Catalog No.T8021 and Catalog No. F8051). In vivo anti-mouse PDL1 antibody purchased from BioXell (B7-H1, catalogue No. BE0101).

Cell lines and laboratory animals
The 4T1 and MCF-7/ADR cell lines were originally obtained from the American Type Culture Collection (ATCC). All cells were cultured in RMPI 1640 medium (Solarbio) containing 1% penicillin (HyClone), 1% streptomycin (HyClone) and 10% fetal bovine serum (FBS, Sigma). Female BALB/c mice (4–6 weeks) were purchased from Shanghai Sakas Biotechnology Co., Ltd. Mice were housed in a pathogen-free SPF room at 20 ± 3 °C, 40–70% relative humidity, and a 12-h light/dark cycle. All animal experiments were performed in accordance with national Ministry of Health guidelines and protocols approved by the Experimental Animal Center of Shanghai Tenth People's Hospital.

Synthesis of FeOX NPs
FeMOF nanoparticles were synthesized by a solvothermal reaction. Generally, FeCl$_3$-6H$_2$O (2250 mg) was dissolved in 15 ml DMF and 2-aminoterephthalic acid (450 mg) was dissolved in 15 mL DMF and dissolved by sonicate, then FeCl$_3$-6H$_2$O was added dropwise to
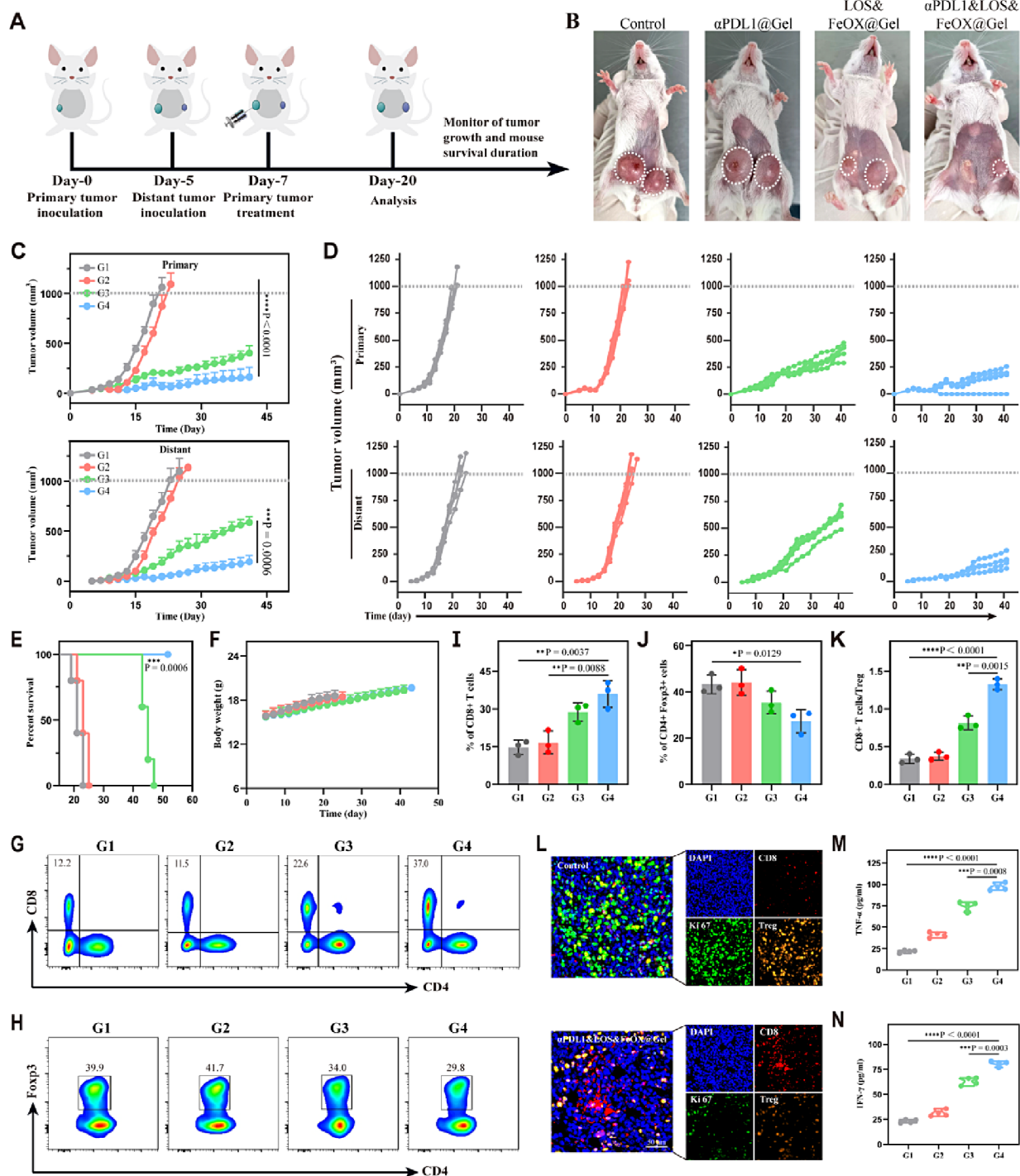
Fig. 6 LOS&FeOX@Gel renders post-chemotherapy tumor responsive to checkpoint immunotherapy. (**A**) Schematic diagram of the in vivo treatment schedule on tumor bearing model with bilateral tumors. (**B**) Representative photographic imaging of different groups of mice after 14 days of varied treatments. (**C-F**) Mean tumor growth curves (**C**), individual tumor growth kinetics (**D**), Kaplan-Meier survival curves (**E**), body weight fluctuation curves (**F**) in tumor-bearing mice after varied treatments ($n=5$ mice in C-F). (**G, H**) FCM analysis of the frequency of CD8+T cells in CD45$^+$CD3$^+$ cells (**G**) and CD4$^+$Foxp3$^+$ Treg cells in CD3$^+$ cells (**H**) in distant tumors after varied treatments. (**I-K**) Quantification by FCM of CD8$^+$ T cells (**I**), CD4$^+$Foxp3$^+$ Treg cells (**J**) and CD8/Treg (**K**) ratios. (**L**) Representative mIHC staining images of distant tumor tissue sections with DAPI (blue), CD8$^+$ T (red), Treg(yellow) and Ki67(green) cell infiltration in tumors after varied treatments. (**M, N**) Cytokine levels of TNF-α (**M**) and IFN-γ (**N**) in the serum after varied treatments ($n=4$). G1, Control; G2, αPDL1@Gel; G3, LOS&FeOX@Gel; G4, αPDL1&LOS&FeOX@Gel. E, Survival analysis determined by the log-rank (Mantel-Cox) test. I, J,K, M,N, Data are presented as the mean±SD. Statistical significance was calculated by the two-tailed unpaired Student's t-test. *$P<0.05$, **$P<0.01$, ***$P<0.001$,****$P<0.0001$

2-aminoterephthalic acid, stirred for 30 min, in The FeMOF NPs were obtained in a teflon lined autoclave, after centrifugation at 120 ℃, 24 h. Then 13,000 rpm for 15 min, washed twice with ethanol and deionised water, respectively, and finally redispersed in ethanol (10 mL). FeMOF (4 mg) and NHS-PEG-MAL (50 mg) were mixed in MES buffer pH=6.0 and reacted for 2 h at room temperature, followed by centrifugation for surface grafting of RGD peptides. The c(RGDyC) peptide (4 mg mL^{-1}) was then added to the FeMOF suspension and further reacted for 2 h. The RGD-grafted FeMOF NPs were centrifuged and dispersed in ethanol (10 mL) containing free OX (15 μg) and rotary evaporated at 30 °C. The finished product was washed with deionised water and then collected for further analysis and application, and the loading efficiency of OX within FeMOF was determined by high performance liquid chromatography (HPLC).

Characterizations
The morphology and elemental composition of the nanoparticles were observed by transmission electron microscopy (TEM, FEI Tecnai G2 F30). Particle size and zeta potential were measured using a Zetasizer Nano ZS90 laser particle size analyzer. The valence state of Fe, N, C, O were analyzed by X-ray photoelectron spectroscopy (XPS, Thermo scaleb 250Xi). X-ray diffraction (XRD) was performed in Riraku D/MAX-2550 V medium under the influence of Cu-Ka radiation.

Degradation assay of FeMOF NPs in vitro
20 mg of FeMOF was placed into 10 mL of phosphate buffer solution (pH 7.4; pH 6.4, with or without 20 mM GSH) and agitated at 37 °C. At designated time points (0, 2, 4, 8, 12, and 24 h), the mixture was centrifuged, and 1 mL of the supernatant was harvested. The cumulative release of iron ions was quantified utilizing ICP-MS.

Formation of Fibrin Gel
Dissolve thrombin (500 IU/ml) in deionized water or PBS (comprising 26 mg/L NaCl and 7 mg/L CaCl$_2$). Dissolve 50 mg/ml fibrinogen solution in deionized water or PBS and sonicate for 3 min. Then, heat the fibrinogen solution at 37 °C for 30 min to dissolve the required amount of FeOX or LOS in the fibrinogen solution. Mix thrombin and fibrinogen solutions (with or without drug) in a 1:2 volume ratio using a dual syringe to form the fibrin gel in situ.

Characterisation of fibrin gels
Fibrin gels were frozen overnight at -80℃ and then the microstructure of the gels was inspected by cryo-SEM (SU8010). The dynamic rheology of the fibrin gel was measured at 25℃ using an advanced rotational rheometer (HAAKE MARS 60) with a 20 mm cross-etched aluminum plate.

Bio-degradability and bio-compatibility of fibrin gels in vitro and in vivo
For in vitro degradation behaviour, fibrin gel was added to PBS and photo-recorded on days 0, 1, 3, 7, 14, 21 to observe gel degradation. For in vivo bio-degradable and bio-compatible behaviour, fibrin gel was injected into the subcutaneous tissue of the abdominal cavity of BALB/c mice (200 μL per sample) and executed at 0, 1, 3, 7, 14, 21 and 28 day. The bio-degradation of the fibrin gel was photo-recorded, while H&E staining of the surrounding skin was performed to observe the bio-compatibility of the tissue.

Drug release from fibrin gel
In vitro experiments were performed in neutral PBS at 37℃ for drug release assays. Fibrin gels were loaded with LOS, and samples were collected at different time points to evaluate the drug release characteristics of LOS from fibrin gels by UV-Vis spectrophotometry. To assess the in vivo drug release behavior, ICG with or without fibrin gels (free ICG and ICG@Gel) were injected into the subcutaneous tissue of the peritoneal cavity of BALB/c mice. Then monitored and quantified the fluorescence intensity at different time points utilising the IVIS imaging system.

Cellular uptake evaluation of nano formulations
MCF-7/ADR cells were inoculated at a density of 1×10^5 into confocal culture dishes and incubated overnight in medium. The medium was then replaced with fresh medium containing PBS, FITC-labelled FeMOF, FeMOF/OX and FeOX (100 μg mL^{-}) and incubated for another 24 h. The cells will be incubated with Typan blue to quench cytoplasmic fluorescence, then washed 3 times with PBS, fixed in paraformaldehyde for 30 min at 4℃ and washed 3 times with PBS. The nuclei were stained with DAPI for 5 min. The stained cells were washed 3 times with PBS and fixed in glycerol before CLSM observed afterward.

Quantification of intracellular iron levels
MCF-7/ADR cells were inoculated at a density of 1×10^5 onto 6 well plates overnight and the previously added medium was replaced with new medium containing PBS, FeMOF, FeMOF/OX and FeOX (100 μg mL^{-1}) and incubation continued for 12–24 h. Subsequently, the medium was removed and washed 3 times with PBS. The cells were digested with EDTA-free trypsin, then purified 2 times by repeated centrifugation and finally lysed by adding cell lysis solution and the resulting solution was sonicated 10 min to ensure competitive cell disintegratio. The solutions obtained were used for ICP assays.

Evaluation of ICD expression

MCF-7/ADR cells were inoculated at a density of 1×10^3 in Nunclon Sphera microplate for 48 h to purchase multicellular spherical cells. The formed multicellular spherical cells were co-incubated with PBS, FeMOF, FeMOF/OX and FeOX (100 µg mL^{-1}) for 12 h. Then cells were washed 3 times with PBS, incubated for 1 h with HMGB1 (CST, Catalog No. 3935, diluted at 1:500), CRT (CST, D3E6, Catalog No. 12238, diluted at 1:1000) monoclonal antibodies, and stained with goat anti-rabbit IgG H&L (Alexa Fluor® 488) or goat anti-rabbit IgG H&L (Alexa Fluor® 555) for another 1 h, DAPI stained for 20 min before CLSM observed afterward.

Cell viability assay

MCF-7/ADR cells were inoculated in 96-well plates at a density of 5×10^3 cells/well and incubated for 12 h to allow complete cell wall attachment. The medium was replaced with fresh medium containing FeMOF, OX, FeMOF/OX, FeOX (0, 25, 50, 75, 100, 150, 200 µg mL^{-1}) and incubated for 24 h before performing the CCK-8 assay.

Live/dead cell staining assay

MCF-7/ADR cells were inoculated at a density of 1×10^5 into confocal culture dishes overnight, then treated with PBS, FeMOF, OX, FeMOF/OX and FeOX (100 µg mL^{-}). After 24 h incubation, the cells were stained with Calcein-AM and PI solutions for 30 min. Finally, the cells were washed three times with PBS and then visualised by CLSM.

Toxicological evaluation in vivo

Female BALB/c mice (4–6 weeks) were divided into two groups and injected with PBS or FeOX/LOS@Gel subcutaneously. On days 10 and 20, serum were collected for blood biochemistry analysis, and major organs were extracted for H&E staining.

Tumor models and treatment trials

To construct a unilateral post-chemotherapy TNBC tumor model, a density 1×10^6 4T1 cells were injected subcutaneously into the fat pad of the right breast of female BALB/c mice (4–6 weeks), tail vein doxorubicin (dose 5 mg kg^{-1}) was given once a week for 3–4 months. The tumor grew slowly to become larger and then gradually smaller. Thereafter, the extracted tumor was divided into subcutaneous implants of approximately 5 mm in diameter and placed into the fat pad of the right breast of female BALB/c mice (4–6 weeks).

To estimate the difference in tumor stiffness between TNBC and post-chemotherapy TNBC, ultrasound SWE imaging was performed every two days when the TNBC and post-chemotherapy TNBC, tumor volumes reached 100 mm^3 and the tumor growth curve was recorded. A region of interest (ROI) of 1 mm diameter was selected from the three stiffest segments during ultrasound SWE to measure the stiffness values and mean values were calculated. The mouse SWE imaging performer was a specialist sonographer with over 5 years of clinical experience. The difference in SWE imaging stiffness was greatest when the tumor reached 800 mm^3, the mice were euthanised, the tumor extracted and weighed. A portion of the isolated tumor was excised for AFM evaluation and another portion was taken for RNA sequencing.

To evaluate the sustained release of losartan reduce the solid pressure in post-chemotherapy TNBC mice, post-chemotherapy TNBC mice were randomly divided into control, single free LOS, sequential free LOS and LOS@ Gel groups. When the tumor volume reached 50 mm^3, each group was injected with PBS, LOS, sequential free LOS (3 times, every 2 days) or LOS@Gel (LOS=60 mg kg^{-1}) peritumorally. SWE imaging was performed every two days after treatment, and the tumor size and body weight were measured. When the tumors reached 800 mm^3, mice were euthanised, tumors were extracted and weighed. A portion of the isolated tumor was excised for AFM evaluation and another portion was taken for mIHC staining.

To investigated the efficacy of combination therapy in unilateral tumors, post-chemotherapy TNBC were randomly divided into control groups, FeMOF@Gel, LOS@ Gel, FeOX@Gel, FeOX/LOS@Gel, and when the tumor volume reached 50 mm^3, each group was injected peritumorally with PBS, FeMOF@Gel, LOS@Gel, FeOX@Gel, FeOX/LOS@ Gel (OX=10 mg kg^{-1}, LOS=60 mg kg^{-1}). Tumor size and body weight were measured every two days after treatment. Mice were euthanised when there were tumors that reached 1000 mm^3 in size or showed signs of cachexia.

To investigated the efficacy of combination therapy in bilatera tumors, distal tumors (5 mm tumor masses) were grafted to the left side of female BALB/c mice 5 days after inoculation of the right side tumor (4–6 weeks) and randomly divided into control groups, aPDL1, LOS &FeOX@Gel, αPDL1&LOS &FeOX@Gel, and when the right tumor volume reached 50 mm^3, each group was peritumorally injected on the right tumor with PBS, aPDL1, LOS &FeOX@Gel, αPDL1&LOS &FeOX@Gel (aPDL1=3.75 mg kg^{-1}, OX=10 mg kg^{-1}, LOS=60 mg kg^{-1}). Bilateral tumor size and mouse weight were measured every two days after treatment. Mice were euthanised when there were tumors that reached 1000 mm^3 in size or showed signs of cachexia.

Flow cytometry analysis

The tumor tissues were individually digested into suspensions of single cells and were initially incubated at a

temperature of 4 °C for a duration of 15 min with anti-CD16/32 (eBioscience, FRC-4G8, Catalog No. MFCR00) monoclonal antibody to prevent any non-specific binding. Subsequently, the cells were stained using diluted fluorescent antibodies that were chromium-coupled. The antibodies utilized in these experiments included CD45-eF506 (eBioscience, 30-F11, Catalog No. 69-0451-82), CD4-FITC (eBioscience, GK1.5, Catalog No. 1-0041-82), CD8-Percpcy5.5 (eBioscience, 53−6.7, the Catalog No. 45-0081-82), Foxp3-PE (eBioscience, N418, Catalog No. 12-0114-82). Additional reagents, such as the erythrocyte lysis buffer (Catalog No. 0-4300-54), intracellular fixation/perm buffer set (Catalog No. 88824-00), and Foxp3 Transcription Factor Staining Buffer Set (Catalog No. 0-552300), were obtained from Thermo. For each experiment, the antibodies were appropriately diluted to achieve a working concentration of 0.2 µg. Finally, the stained cells were filtered and subjected to detection using FACS FCM (BD, Fortessa X20). The resulting data were then analyzed using Flowjo software (TreeStar, 10.6.2).

Immunohistochemistry (IHC)

To estimate the difference in tumor stiffness between TNBC and PC-TNBC, when the tumor reached 800 mm^3, the mice were euthanised, the tumor extracted and a portion of the isolated tumor was excised for IHC staining. The tumor tissue samples were immersed in a solution of 4% (v/v) paraformaldehyde in PBS for a duration of 10 min at room temperature to ensure fixation. After overnight incubation with primary antibodies α-SMA-Cy3™ (Sigma-Aldrich, Catalog No. C6198, diluted at 1:200), collagen-I (abcam; Catalog No. ab270993, diluted at 1:500) at 4 °C, the sections were exposed to 0.3% H_2O_2 in TBS for 15 min at room temperature. And then the sections were incubated with secondary antibodies diluted 1:500 in TBS containing 10% FBS for 1 h at room temperature. Sections were then incubated with 3,3'-diaminobenzidine (DAB) to generate signal and counterstained with hematoxylin. After dehydration and mounting, tissue sections were scanned using a Leica SCN400 slide scanner.

Immunofluorescence staining

Tumors were isolated and collected from mice, and tumor sections were stained according to the instructions of the Fluorescent Immunohistochemical Staining Kit (Absin, Catalog No.abs50013). Antibodies involved in the experiments included α-SMA-Cy3™ (Sigma-Aldrich, Catalog No. C6198, diluted at 1:200), collagen-I (abcam; Catalog No. ab270993, diluted at 1:500), CD31 (abcam, Catalog No.ab28364, diluted at 1:100), HMGB1 (CST, Catalog No. 3935, diluted at 1:100), calreticulin (CST, D3E6, Catalog No. 12238, diluted at 1:500), Ki67 (abcam;

Catalog No. ab15580, diluted at 1:5000), Foxp3 (abcam, Catalog No. ab215206, diluted at 1:200) CD8 (abcam, Catalog No. ab251596, diluted at 1:5000). Cell nuclei were stained with DAPI prior to sealing and all sections were scanned with a fluorescence scanning camera (KFBIO, KF-TB-400).

Cytokine assay

Mouse serum samples were collected and isolated. Serum TNF-α (Invitrogen, catalog number BMS607-3) and IFN-γ (Invitrogen, catalog number BMS607-3) were analyzed using an ELISA kit and according to the supplier's protocol.

Clinical samples

84 patients with TNBC were recruited from the Shanghai Tenth People's Hospital in Shanghai, and SWE imaging and pathological data were collected from January 2018 to December 2021 for patients before treatment or after surgical resection. This retrospective study was conducted with the informed consent of the patients and approved by the Ethics Commission of the Shanghai Tenth People's Hospital (ChiCTR2000035381).

Statistical analysis

The quantitative data were expressed as mean±SD. Statistical significance was calculated by GraphPad Prism (version 8.0.2) using unpaired student's t-test or one-way analysis of variance (ANOVA) when comparing two or multiple groups, respectively. The survival curve was analyzed by the Log-rank test. All flow cytometry data were analyzed using the FlowJo™ software package (version 10.5.2). P values less than 0.05 were considered significant, $*P < 0.05$, $**P < 0.01$, $***P < 0.001$, $****P < 0.0001$.

Supplementary Information

The online version contains supplementary material available at https://doi.org/10.1186/s12951-024-02871-0.

> Supplementary Material 1

Hou *et al. Journal of Nanobiotechnology*   (2024) 22:667

Page 18 of 19

Data availability
No datasets were generated or analysed during the current study.

Declarations

Ethics approval and consent to participate
All animal experiments were approved by the Laboratory Animal Center in Tenth People's Hospital affiliated from Tongji University School of Medicine with an approval number: SHDSYY-2023-3429-KR0246.

Consent for publication
Written informed consent for publication was obtained from all participants.

Competing interests
The authors declare no competing interests.

Author details
[1]Department of Medical Ultrasound, Center of Minimally Invasive Treatment for Tumor, Shanghai Tenth People's Hospital, School of Medicine, Tongji University, Shanghai 200072, P.R. China
[2]Ultrasound Research and Education Institute, Clinical Research Center for Interventional Medicine, School of Medicine, Tongji University, Shanghai, P.R. China
[3]Shanghai Engineering Research Center of Ultrasound Diagnosis and Treatment, National Clinical Research Center for Interventional Medicine, Shanghai 200072, P.R. China
[4]Department of Ultrasound, Institute of Ultrasound in Medicine and Engineering, Zhongshan Hospital, Fudan University, Shanghai 200032, P.R. China
[5]Department of Ultrasound, Zhejiang Hospital, Hangzhou, Zhejiang Province 310013, P.R. China

References
1. Tang J, Yu JX, Hubbard-Lucey VM, Neftelinov ST, Hodge JP, Lin Y. The clinical trial landscape for PD1/PDL1 immune checkpoint inhibitors. Nat Rev Drug Discov. 2018;17:854–5.
2. Topalian SL, Taube JM, Pardoll DM. Neoadjuvant checkpoint blockade for cancer immunotherapy. Science. 2020;367:x182.
3. Forde PM, Chaft JE, Smith KN, Anagnostou V, Cottrell TR, Hellmann MD, Zahurak M, Yang SC, Jones DR, Broderick S, et al. Neoadjuvant PD-1 blockade in Resectable Lung Cancer. N Engl J Med. 2018;378:1976–86.
4. Topalian SL, Forde PM, Emens LA, Yarchoan M, Smith KN, Pardoll DM. Neoadjuvant immune checkpoint blockade: a window of opportunity to advance cancer immunotherapy. Cancer Cell. 2023;41:1551–66.
5. Shen Y, Chen L, Guan X, Han X, Bo X, Li S, Sun L, Chen Y, Yue W, Xu H. Tailoring Chemoimmunostimulant Bioscaffolds for inhibiting Tumor Growth and Metastasis after Incomplete Microwave ablation. ACS Nano. 2021;15:20414–29.
6. Guan X, Sun L, Shen Y, Jin F, Bo X, Zhu C, Han X, Li X, Chen Y, Xu H, Yue W. Nanoparticle-enhanced radiotherapy synergizes with PD-L1 blockade to limit post-surgical cancer recurrence and metastasis. Nat Commun. 2022;13:2834.
7. Li S, Zhu C, Zhou X, et al. Engineering ROS-Responsive Bioscaffolds for disrupting myeloid cell-driven immunosuppressive niche to enhance PD-L1 blockade-based postablative immunotherapy. Adv Sci (Weinh). 2022;9(11):e2104619.
8. Ribas A, Wolchok JD. Cancer immunotherapy using checkpoint blockade. Science. 2018;359:1350–5.
9. Zhang T, Jia Y, Yu Y, Zhang B, Xu F, Guo H. Targeting the tumor biophysical microenvironment to reduce resistance to immunotherapy. Adv Drug Deliv Rev. 2022;186:114319.
10. Sung H, Ferlay J, Siegel RL, Laversanne M, Soerjomataram I, Jemal A, Bray F. Global Cancer Statistics 2020: GLOBOCAN Estimates of Incidence and Mortality Worldwide for 36 Cancers in 185 Countries. CA: A Cancer Journal for Clinicians 2021, 71:209–249.
11. Emens LA. Breast Cancer Immunotherapy: facts and hopes. Clin Cancer Res. 2018;24:511–20.
12. Zhao Y, Cao J, Melamed A, Worley M, Gockley A, Jones D, Nia HT, Zhang Y, Stylianopoulos T, Kumar AS et al. Losartan treatment enhances chemotherapy efficacy and reduces ascites in ovarian cancer models by normalizing the tumor stroma. Proceedings of the National Academy of Sciences: 2019, 116:2210–2219.
13. Pozzi C, Cuomo A, Spadoni I, Magni E, Silvola A, Conte A, Sigismund S, Ravenda PS, Bonaldi T, Zampino MG, et al. The EGFR-specific antibody cetuximab combined with chemotherapy triggers immunogenic cell death. Nat Med. 2016;22:624–31.
14. Galluzzi L, Humeau J, Buqué A, Zitvogel L, Kroemer G. Immunostimulation with chemotherapy in the era of immune checkpoint inhibitors. Nat Rev Clin Oncol. 2020;17:725–41.
15. Gonzalez-Molina J, Moyano-Galceran L, Single A, Gultekin O, Alsalhi S, Lehti K. Chemotherapy as a regulator of extracellular matrix-cell communication: implications in therapy resistance. Semin Cancer Biol. 2022;86:224–36.
16. Guarin JR, Fatherree JP, Oudin MJ. Chemotherapy treatment induces pro-invasive changes in liver ECM composition. Matrix Biol. 2022;112:20–38.
17. Jain RK. Normalizing Tumor Microenvironment to treat Cancer: bench to bedside to biomarkers. J Clin Oncol. 2013;31:2205–18.
18. Johnston CI. Angiotensin receptor antagonists: focus on losartan. Lancet. 1995;346:1403–7.
19. Stylianopoulos T, Munn LL, Jain RK. Reengineering the physical microenvironment of tumors to Improve Drug Delivery and Efficacy: from Mathematical modeling to bench to Bedside. Trends Cancer. 2018;4:292–319.
20. Nia HT, Liu H, Seano G, Datta M, Jones D, Rahbari N, Incio J, Chauhan VP, Jung K, Martin JD, et al. Solid stress and elastic energy as measures of tumour mechanopathology. Nat Biomed Eng. 2017;1:4.
21. Chauhan VP, Martin JD, Liu H, Lacorre DA, Jain SR, Kozin SV, Stylianopoulos T, Mousa AS, Han X, Adstamongkonkul P, et al. Angiotensin inhibition enhances drug delivery and potentiates chemotherapy by decompressing tumour blood vessels. Nat Commun. 2013;4:2516.
22. Diop-Frimpong B, Chauhan VP, Krane S, Boucher Y, Jain RK. Losartan inhibits collagen I synthesis and improves the distribution and efficacy of nanotherapeutics in tumors. Proc Natl Acad Sci U S A. 2011;108:2909–14.
23. Yue W, Chen L, Yu L, Zhou B, Yin H, Ren W, Liu C, Guo L, Zhang Y, Sun L et al. Checkpoint blockade and nanosonosensitizer-augmented noninvasive sonodynamic therapy combination reduces tumour growth and metastases in mice. Nat Commun 2019, 10.
24. Gong F, Cheng L, Yang N, Gong Y, Ni Y, Bai S, Wang X, Chen M, Chen Q, Liu Z. Preparation of TiH1.924 nanodots by liquid-phase exfoliation for enhanced sonodynamic cancer therapy. Nat Commun. 2020;11:3712.
25. Feng C, Ouyang J, Tang Z, Kong N, Liu Y, Fu L, Ji X, Xie T, Farokhzad OC, Tao W. Germanene-based Theranostic materials for Surgical Adjuvant Treatment: inhibiting Tumor recurrence and wound infection. Matter. 2020;3:127–44.
26. Gong N, Zhang Y, Teng X, Wang Y, Huo S, Qing G, Ni Q, Li X, Wang J, Ye X, et al. Proton-driven transformable nanovaccine for cancer immunotherapy. Nat Nanotechnol. 2020;15:1053–64.
27. Rosenberg SA, Restifo NP. Adoptive cell transfer as personalized immunotherapy for human cancer. Science. 2015;348:62–8.
28. Han X, Li H, Zhou D, Chen Z, Gu Z. Local and targeted delivery of Immune Checkpoint Blockade therapeutics. Acc Chem Res. 2020;53:2521–33.
29. Saatci O, Kaymak A, Raza U, Ersan PG, Akbulut O, Banister CE, Sikirzhytski V, Tokat UM, Aykut G, Ansari SA, et al. Targeting lysyl oxidase (LOX) overcomes chemotherapy resistance in triple negative breast cancer. Nat Commun. 2020;11:2416.
30. Park CG, Hartl CA, Schmid D, Carmona EM, Kim H, Goldberg MS. Extended release of perioperative immunotherapy prevents tumor recurrence and eliminates metastases. Sci Transl Med. 2018;10:r1916.
31. Hu C, Liu X, Ran W, Meng J, Zhai Y, Zhang P, Yin Q, Yu H, Zhang Z, Li Y. Regulating cancer associated fibroblasts with losartan-loaded injectable peptide hydrogel to potentiate chemotherapy in inhibiting growth and lung metastasis of triple negative breast cancer. Biomaterials. 2017;144:60–72.
32. Liu L, Chen J, Bae J, Li H, Sun Z, Moore C, Hsu E, Han C, Qiao J, Fu Y. Rejuvenation of tumour-specific T cells through bispecific antibodies targeting PD-L1 on dendritic cells. Nat Biomed Eng. 2021;5:1261–73.
33. Song Q, Han L, Mao Y, Huang T. An investigation on biomarkers of hyperprogressive disease after PD-1/PDL-1 therapies in Chinese non-small cell lung cancer patients. J Clin Oncol. 2021;39:e21173.

34. Chen Y, Zander RA, Wu X, Schauder DM, Kasmani MY, Shen J, Zheng S, Burns R, Taparowsky EJ, Cui W. BATF regulates progenitor to cytolytic effector CD8+T cell transition during chronic viral infection. Nat Immunol. 2021;22:996–1007.

35. Garassino MC, Cho B, Kim J, Mazières J, Vansteenkiste J, Lena H, Corral Jaime J, Gray JE, Powderly J, Chouaid C, et al. Durvalumab as third-line or later treatment for advanced non-small-cell lung cancer (ATLANTIC): an open-label, single-arm, phase 2 study. Lancet Oncol. 2018;19:521–36.

36. Wang S, McGuirk CM, D'Aquino A, Mason JA, Mirkin CA. Metal–Organic Framework nanoparticles. Adv Mater. 2018;30:1800202.

37. Wang L, Lu D, Huo M, Xu H. Oligomycin a induces apoptosis-to-pyroptosis switch against Melanoma with Sensitized Immunotherapy. Adv Funct Mater. 2022;32:2106332.

38. Wan X, Song L, Pan W, Zhong H, Li N, Tang B. Tumor-targeted Cascade Nanoreactor based on Metal-Organic frameworks for synergistic ferroptosis-starvation anticancer therapy. ACS Nano. 2020;14(9):11017–28.

39. Ma Y, Adjemian S, Mattarollo SR, Yamazaki T, Aymeric L, Yang H, Portela Catani JP, Hannani D, Duret H, Steegh K, et al. Anticancer Chemotherapy-Induced Intratumoral recruitment and differentiation of Antigen-presenting cells. Immunity. 2013;38:729–41.

40. Apetoh L, Ghiringhelli F, Tesniere A, Obeid M, Ortiz C, Criollo A, Mignot G, Maiuri MC, Ullrich E, Saulnier P, et al. Toll-like receptor 4–dependent contribution of the immune system to anticancer chemotherapy and radiotherapy. Nat Med. 2007;13:1050–9.

41. Chao Y, Liang C, Tao H, Du Y, Wu D, Dong Z, Jin Q, Chen G, Xu J, Xiao Z, et al. Localized cocktail chemoimmunotherapy after in situ gelation to trigger robust systemic antitumor immune responses. Sci Adv. 2020;6:z4204.

42. Waks AG, Winer EP. Breast Cancer Treatment: a review. JAMA. 2019;321:288–300.

43. Sato K, Padgaonkar AA, Baker SJ, Cosenza SC, Rechkoblit O, Subbaiah DRCV, Domingo-Domenech J, Bartkowski A, Port ER, Aggarwal AK et al. Simultaneous CK2/TNIK/DYRK1 inhibition by 108600 suppresses triple negative breast cancer stem cells and chemotherapy-resistant disease. Nat Commun 2021, 12.

Publisher's note